IV International Conference on Simulation for Additive Manufacturing
Sim-AM 2023
E. Rank and S. Kollmannsberger (Eds)

THERMAL MODEL FOR LASER-BASED POWDER BED FUSION OF METAL PROCESS: MODELLING, CALIBRATION, AND EXPERIMENTAL VALIDATION

Massimo Carraturo*, Philipp P. Breese† and Simon Oster†

*Department of Civil Engineering and Architecture, University of Pavia,
via Ferrata 3, 27100 Pavia, Italy
e-mail: massimo.carraturo@unipv.it

†Bundesanstalt für Materialforschung und-Prüfung (BAM, Federal Institute for Materials Research and Testing),
Unter den Eichen 87, 12205 Berlin, Germany
e-mail: philipp-peter.breese@bam.de, simon.oster@bam.de

Key words: Laser powder bed fusion of metals, melt pool measurements, experimental validation, thermal analysis, SS 316L

Abstract. In the present contribution, we propose an effective numerical thermal modeling solution for melt pool simulations in Laser-based Powder Bed Fusion of Metals processes. The proposed model employs an anisotropic conductivity to represent melt pool dynamics effects in a homogeneous material model. The numerical implementation of the proposed physical model is first experimentally calibrated and then validated with respect to a series of melt pool measurements as acquired by using a short-wave infrared (SWIR) camera monitoring system.

1 Introduction

Laser-based Powder Bed Fusion of Metals (PBF-LB/M) has known exponential growth over the last decades due to its capacity to produce close-to-freeform designs with high accuracy and mechanical properties that for bulk material components are comparable to subtractive manufacturing technologies [20]. Stainless steel 316L (SS 316L) is a common steel in Additive Manufacturing (AM) applications, due to its high strength-to-weight ratio, excellent durability, hardness, and mechanical properties at high temperatures. For instance, it can be used for the production of engine components in the aerospace and automotive industry, as well as for hydraulic components, heat exchangers, and structural joints.

Numerical methods can be a valid solution to predict the temperature field evolution during the PBF-LB/M process. In the literature, several contributions can be found presenting a broad set of thermal models and employing different numerical techniques [19, 5]. More specifically, thermal models for PBF-LB/M process simulations can be divided into two main groups: i) models which consider the single powder particles and melt pool dynamics [10] and ii) models which consider the different phases of the material as homogeneous media [14]. The latter is a well-established approach in the literature for meso and part-scale thermal analysis [2, 17, 6]. For a detailed review of the state of the art of PBF-LB/M thermal simulations, we refer to [21].

In the present contribution, we propose a heat transfer model with homogeneous material, extending the modeling solution proposed in [11]. The simulated melt pool area, length, and width are compared to SWIR-measured data for the corresponding physical process, showing excellent agreement between numerical and experimental results.

2 Physical and numerical model

Following [8], let us consider a physical domain $\Omega \subset \mathbb{R}^3$ with homogeneous material. In such a domain, we want to solve a heat conduction problem, i.e., a problem describing the physical phenomena occurring during the PBF-LB/M process.

Let T indicate the temperature field, the heat conduction problem can be written as:

$$\rho c_p \dot{T} - \nabla \cdot (k \nabla T) = Q \qquad \text{in } \Omega, \tag{1}$$

$$k \nabla T = q \qquad \text{on } \partial\Omega, \tag{2}$$

$$T = T_0 \qquad \text{at } t = 0, \tag{3}$$

with $k = k(T)$ the temperature-dependent thermal conductivity of the material, $\rho = \rho(T)$ the temperature-dependent density of the material, and $c_p = c_p(T)$ the temperature-dependent specific heat capacity, Q the rate of heat per unit volume, q a prescribed heat flux on the domain boundaries, and T_0 the initial temperature in Ω. The Gaussian model proposed by [7] is used to model the heat source energy input term Q, as follows:

$$Q(x, y, z, t) = \frac{6\sqrt{3}P\eta}{\pi\sqrt{\pi}r^2 d} e^{-3\left[\frac{(x-x_c)^2}{r^2} + \frac{(y-y_c)^2}{r^2} + \frac{(z-z_c)^2}{d^2}\right]}, \tag{4}$$

where P is the laser power, η is the absorptivity of the material, r the laser radius, and d the laser penetration depth parameter with the laser beam centered in $[x_c, y_c, z_c]$.

2.1 Boundary conditions

The PBF-LB/M process occurs within a closed build chamber where an inert gas (argon) flux is present to dissipate heat by convection. At the same time, heat is dissipated by radiation in the region surrounding the melt pool due to the high temperature generated by the localized laser beam. Therefore, the heat flux q in Eq. (2) models these two heat loss mechanisms on the upper surface of the domain and it is defined as:

$$q = q_c + q_r \tag{5}$$

where q_c is the heat loss by convection and q_r is the heat loss by radiation on the upper surface of the domain Ω. These two terms are defined as follows:

$$q_c = h_c(T_a - T) \qquad \text{and} \qquad q_r = \sigma_{sb}\epsilon(T_a^4 - T^4) \tag{6}$$

with h_c the convection coefficient, T_a the the ambient temperature in the build chamber, σ_{sb} the Stefan-Boltzmann constant, and ϵ the emissivity of the material.

2.2 Material model

The material considered in the present work is AISI SS 316L, a common steel in AM applications. The temperature dependent parameters are taken from [4], while, following [15], the convection coefficient value, h_c is set to 14.5 [W/m^{2}K].

In the present work, a homogenized material is employed to model the problem, i.e., the liquid phase of the material is a solid material with different thermal properties. Such an approach is very common in the literature; however, it does not allow us to consider the melt pool dynamics and its influence on the temperature distribution. In [9] and [11], an anisotropic enhanced thermal conductivity approach is used to model melt pool dynamics influence on the temperature distribution in the melt pool neighborhood.

In the present work, the thermal conductivity of the material is scaled by a conductivity scaling factor diagonal matrix ϑ_i, with $i = x, y, z$. Such a scaling factor is applied at high temperatures, i.e., the thermal material conductivity is modified at temperatures above a temperature T_k close to the melting temperature ($T_k = 1200$°C). In particular, we consider an anisotropic scaling factor $\vartheta_z = \vartheta_y = 0.5\vartheta_x$ for the homogeneous thermal conductivity of the material $k = k(T)$ when $T > T_k$, modifying Eq. (2) such that:

$$\rho c_p \dot{T} - \frac{\partial}{\partial x}\left(\vartheta_x k \frac{\partial T}{\partial x}\right) - \frac{\partial}{\partial y}\left(\vartheta_y k \frac{\partial}{\partial y}\right) - \frac{\partial}{\partial z}\left(\vartheta_z k \frac{\partial}{\partial z}\right) = Q \tag{7}$$

2.3 Numerical implementation

In the present work, the domain Ω is discretized using a uniform cartesian grid with tri-linear hexahedral elements with dimension $(25 \times 25 \times 25)\,\mu$m^3. To accurately evaluate the computed melt pool morphology, a finer grid is used to post-process the temperature field on the upper surface of the domain. Such a post-processing grid has cells with dimension $(5 \times 5 \times 5)\,\mu$m^3. The melt pool area, length, and width are obtained by setting a threshold on such a post-processing grid and considering only cells with an average temperature above the solidification temperature T_m of the material ($T_m = 1375$°C).

An implicit Euler time integration scheme is used in our implementation to approximate the temperature evolution in time. By following [12], the time step increment Δt is defined as:

$$\Delta t = \frac{r}{v} \tag{8}$$

with v the laser speed, i.e., such that the laser beam moves by a distance equal to the laser spot radius at each time step.

3 Experimental setup

Single track melt pool measurements were performed on a custom PBF-LB/M printer located at the Federal Institute for Materials Research and Testing in Berlin, Germany (see Fig. 1). The printer consists of a recipient with an integrated PBF-LB/M powder bed module. The recipient can be evacuated and filled with inert process gas (argon). Using a focusing unit (varioSCAN, SCANLAB, Puchheim, Germany), and a galvanometer scanner (intelliSCAN, SCANLAB, Puchheim, Germany), a 500 W fiber laser (1070 nm, IPG Photonics, Burbach, Germany) is guided onto the build plate. A dichroic mirror is integrated into the laser path which specifically reflects the laser wavelength. Thereby, a portion of the process emissions is

decoupled and can be used for on-axis measurements of melt pool radiosity. A laser diameter of 46 μm in the focal plane was measured using an optical focal spot analyzing device (Ophir Optronics Solutions, North Logan, USA).

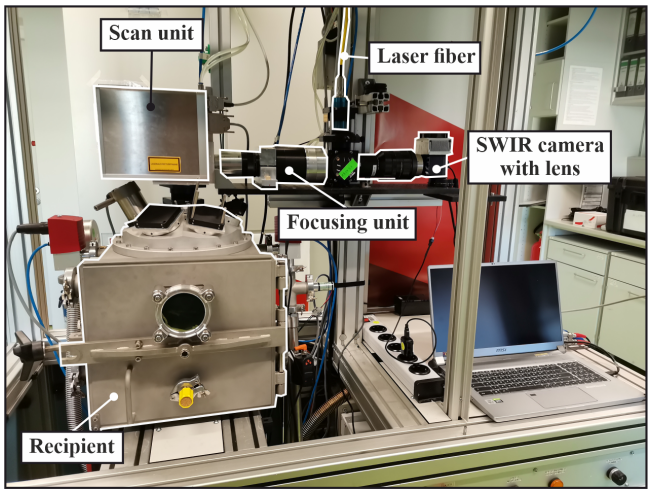

Figure 1: Custom PBF-LB/M printer located at Federal Institute for Material Research and Testing in Berlin, Germany.

For the measurement of the melt pool radiosity, a short-wave infrared (SWIR) camera (C-Red 3, First Light Imaging, Meyreuil, France) in combination with a 100 mm lens was connected to the beam splitter. To neglect a disruptive influence from the laser, a notch filter (1064 ± 2 nm) and a bandpass filter (1500 ± 15 nm) were additionally mounted in front of the lens. The measurement conditions lead to a spatial resolution of 29 μm/pixel in the focal plane. The camera was operated at an acquisition frequency of 9501 Hz in subframe mode with an image size of (64 x 64) pixels. Furthermore, an integration time of 11.6 μs was used. The laser spot position on the focal plane was derived from the mirror position in the scanning unit with a frequency of 100 kHz.

Single tracks were produced on a sandblasted bare plate from AISI SS 316L. We used nine different combinations of laser power P and scan velocity V to produce a variety of melt pool geometries. For each combination, eight scan tracks (length of 15 mm) with a lateral displacement of 0.5 mm were produced. In order to calibrate the thermal model, we produced an additional set of single tracks using an independent parameter set. All parameter combinations are shown in Table 1.

3.1 Image processing

The acquired thermograms were temperature calibrated using a single-point calibration model [18]. The melt pool shape was measured using a blob detection algorithm from *Matlab Image Processing Toolbox* (MathWorks, Natick, MA, US). A global threshold was applied to all thermograms. As threshold value, the solidification temperature T_m was used to separate the liquid material of the melt pool from solidified material. During the blob analysis, the melt pool shape was approximated by an ellipsis. The lengths of the main axes were used to calculate the melt pool length (L) and width (W). In terms of melt pool area (A), the number

of melt pool pixels was summed up.

To estimate the total uncertainty in the melt pool geometry measurements, the uncertainty resulting from single-point calibration was considered. In order to generate a calibration model, a reference intensity I_{ref} was extracted manually from the solidification plateau in the melt pool rear in randomly chosen thermograms. From the measured values, we calculated the standard deviation $\sigma_{I_{ref}}$. A numerical Monte Carlo simulation-based approach was used to incorporate $\sigma_{I_{ref}}$ into the total measurement uncertainty. This method was implemented according to the "Guide to the expression of uncertainty in measurement" (GUM) [3]. We used a Gaussian distribution as probability density function (PDF) for I_{ref}. 1000 random values were drawn from the PDF and propagated through the entire image processing workflow. From all obtained results in terms of A, L and W, we calculated total standard uncertainties in the form of the standard deviation.

Experiment	1	2	3	4	5	6	7	8	9	10
Laser power P [W]	314	314	314	245	245	245	176	176	176	224
Scan velocity V [mm/s]	600	800	1000	600	800	1000	600	800	1000	700

Table 1: Manufacturing parameters for the production of single tracks. The tenth parameter set was used to calibrate the thermal model.

4 Results and discussion

The results presented in this section have been obtained using an Intel® Xeon® W-2125 CPU @ 4.00GHz with 256Gb RAM. The thermal model has been implemented in *AdhoC++*, a numerical framework continuously developed at the Technical University of Munich [22, 13].

4.1 Thermal model calibration

The thermal model described in Section 2 includes numerical parameters that are complex or even impossible to be measured. For these problem parameters, an experimental calibration is required. In the model introduced in Section 2, we consider the following unknown quantities to be calibrated: the material absorptivity η, the conductivity scaling factor along the laser moving direction ϑ_x, and the laser penetration depth d. To calibrate and validate the proposed model, we consider three quantities of interest (QoIs), namely the melt pool area, length, and width. These three QoIs have been considered since they can be measured *in-situ* by means of the SWIR camera mounted on the 3D printing system (see Section 3).

To calibrate the model, we use the *Sparse Grid Matlab Kit* [1, 16] a lightweight, high-level Matlab toolkit for uncertainty quantification analysis based on sparse grids. Sparse grids are a flexible numerical tool suitable for surrogate model generation. They have been proven particularly effective for the generation of surrogate models in low-dimensional parametric space, i.e., when the number of parameters is lower than four.

In the present work, first we perform a global sensitivity analysis to evaluate the sensitivity of our model with respect to variations of the model parameters to be calibrated. Such an analysis shows that the influence of the laser penetration depth on our QoIs is negligible; therefore, in the subsequent calibration and model validation, we keep this parameter fixed, such as $d = 50\mu$m. With the remaining two uncertain variables, we finally construct a surrogate

model to effectively compute problem minimization. The final calibrated parameter values are $\eta = 0.21$ and $\vartheta_k = 3.17$.

4.2 Thermal model validation

To evaluate the robustness of the previously calibrated model, we run a set of nine simulations using the process parameters reported in Table 1. Figure 2 shows the comparison of numerical and experimental evaluation of the melt pool area, length, and width at steady-state along a single track laser scan path. It can be observed that the proposed numerical model is able to accurately capture the melt pool morphology for a wide range of process parameters. However, for Experiments 8 and 9, the predicted area is outside of the measurement error bars; the simulated melt pool length lies outside the experimental error bars for Experiments 6, 8, and 9; whereas the numerical melt pool width is outside experimental error bars for Experiments 2, 3, 6, and 9.

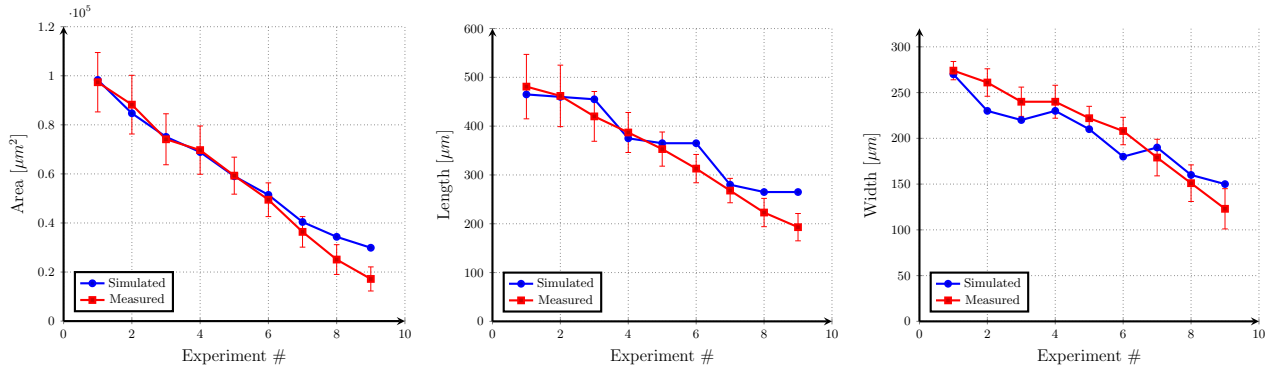

(a) Melt pool area (b) Melt pool length (c) Melt pool width

Figure 2: Melt pool dimensions. Numerical Vs. Experimental results. The shown measurement uncertainties include the uncertainty from thermal calibration.

To better understand the motivation of such a deviation of the numerical model from the experimental data, in Fig. 3 we plot the melt pool area, length, and width with respect to the linear energy density of each experimental setup, defined as $E_l = P/v$. This plot indicates that the proposed model is able to well approximate melt pool behavior not only close to the calibration point, but also for higher linear energy density values. Contrary, when the energy density of the process is much lower than the value used for model calibration, the predicted results start to deviate from the experimental measurements.

5 Conclusions

A simple yet effective thermal model for melt pool morphology prediction in PBF-LB/M processes has been calibrated and experimentally validated with respect to nine different combinations of laser power and speed. The model shows good agreement with experimental results and it can be considered valid for a wide range of linear energy density values. Further outlook of the present work will aim at applying the proposed thermal model to investigate the influence of process-induced defects on melt pool morphology.

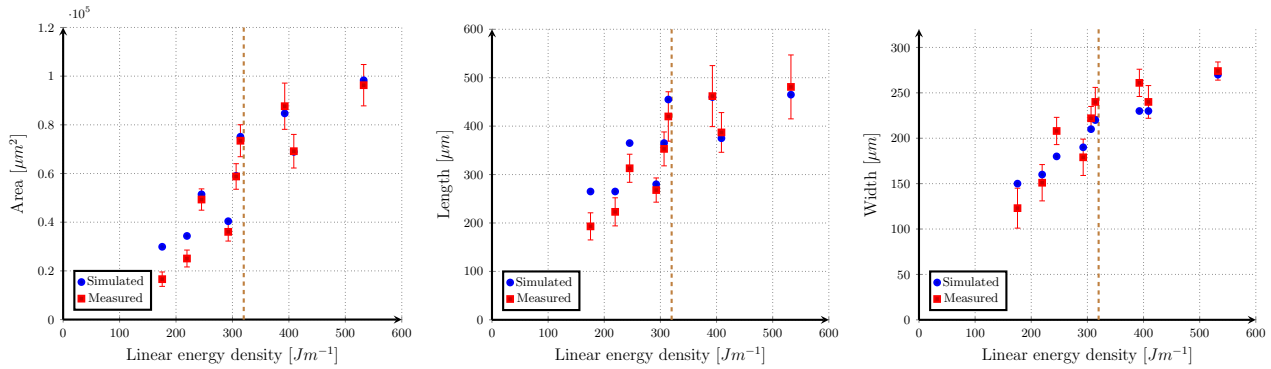

(a) Melt pool area (b) Melt pool length (c) Melt pool width

Figure 3: Melt pool dimensions with respect to linear energy density. Numerical Vs. Experimental results. Dashed lines indicate the linear energy density used for model calibration.

Acknowledgments

This work was partially supported by the Italian Ministry of the University and Research (MUR) through the FSE – REACT EU: PON Ricerca e Innovazione 2014-2020.

REFERENCES

[1] J. Bäck, F. Nobile, L. Tamellini, and R. Tempone. Stochastic spectral Galerkin and collocation methods for PDEs with random coefficients: a numerical comparison. In J. Hesthaven and E. Ronquist, editors, *Spectral and High Order Methods for Partial Differential Equations*, volume 76 of *Lecture Notes in Computational Science and Engineering*, pages 43–62. Springer, 2011. Selected papers from the ICOSAHOM '09 conference, June 22-26, Trondheim, Norway.

[2] J. Baiges, M. Chiumenti, C. A. Moreira, M. Cervera, and R. Codina. An adaptive finite element strategy for the numerical simulation of additive manufacturing processes. *Additive Manufacturing*, page 101650, 2020.

[3] BIPM, IEC, IFCC, ILAC, ISO, IUPAC, IUPAP, and OIML. Evaluation of measurement data — Supplement 1 to the "Guide to the expression of uncertainty in measurement" — Propagation of distributions using a Monte Carlo method. Joint Committee for Guides in Metrology, JCGM 101:2008, https://www.bipm.org/documents/20126/2071204/JCGM_101_2008_E.pdf/325dcaadc15a-407c-1105-8b7f322d651c, 2008. Accessed: 2023-06-23.

[4] M. Boivineau, C. Cagran, D. Doytier, V. Eyraud, M.-H. Nadal, B. Wilthan, and G. Pottlacher. Thermophysical Properties of Solid and Liquid Ti-6Al-4V (TA6V) Alloy. *International Journal of Thermophysics*, 27(2):507–529, 2006.

[5] M. Carraturo, C. Giannelli, A. Reali, and R. Vázquez. Suitably graded thb-spline refinement and coarsening: Towards an adaptive isogeometric analysis of additive manufacturing processes. *Computer Methods in Applied Mechanics and Engineering*, 348:660 – 679, 2019.

[6] E. R. Denlinger, V. Jagdale, G. Srinivasan, T. El-Wardany, and P. Michaleris. Thermal modeling of Inconel 718 processed with powder bed fusion and experimental validation using in situ measurements. *Additive Manufacturing*, 11:7–15, July 2016. 00005.

[7] J. Goldak, A. Chakravarti, and M. Bibby. A new finite element model for welding heat sources. *Metallurgical Transactions B*, 15(2):299–305, June 1984.

[8] J. A. Goldak and M. Akhlaghi. *Computational Welding Mechanics*. Springer, New York, 2005.

[9] A. Kamara, W. Wang, S. Marimuthu, and L. Li. Modelling of the melt pool geometry in the laser deposition of nickel alloys using the anisotropic enhanced thermal conductivity approach. *Proceedings of the Institution of Mechanical Engineers, Part B: Journal of Engineering Manufacture*, 225(1):87–99, 2011.

[10] S. A. Khairallah, A. T. Anderson, A. Rubenchik, and W. E. King. Laser powder-bed fusion additive manufacturing: Physics of complex melt flow and formation mechanisms of pores, spatter, and denudation zones. *Acta Materialia*, 108:36–45, 2016.

[11] S. Kollmannsberger, M. Carraturo, A. Reali, and F. Auricchio. Accurate prediction of melt pool shapes in laser powder bed fusion by the non-linear temperature equation including phase changes. *Integrating Materials and Manufacturing Innovation*, 8:167–177, 2019.

[12] S. Kollmannsberger and P. Kopp. On accurate time integration for temperature evolutions in additive manufacturing. *GAMM-Mitteilungen*, 44(4):e202100019, 2021.

[13] S. Kollmannsberger, A. Özcan, M. Carraturo, J. Egger, A. Schröder, and E. Rank. A multi-level model for the simulation of am processes. volume 2017-October, pages 56–57, 2017.

[14] C. Li, E. R. Denlinger, M. F. Gouge, J. E. Irwin, and P. Michaleris. Numerical verification of an octree mesh coarsening strategy for simulating additive manufacturing processes. *Additive Manufacturing*, 30:100903, 2019.

[15] L. A. Parry. *Investigation of Residual Stress in Selective Laser Melting*. PhD Thesis, University of Nottingham, 2018.

[16] C. Piazzola and L. Tamellini. The Sparse Grids Matlab kit - a Matlab implementation of sparse grids for high-dimensional function approximation and uncertainty quantification. *ArXiv*, (2203.09314), 2022.

[17] D. Riedlbauer, T. Scharowsky, R. F. Singer, P. Steinmann, C. Körner, and J. Mergheim. Macroscopic simulation and experimental measurement of melt pool characteristics in selective electron beam melting of Ti-6Al-4V. *The International Journal of Advanced Manufacturing Technology*, 88(5-8):1309–1317, Feb. 2017.

[18] N. Scheuschner, A. Strasse, S. J. Altenburg, A. Gumenyuk, and C. Maierhofer. In-situ thermographic monitoring of the laser metal deposition process. In *II International Conference on Simulation for Additive Manufacturing*, 2019.

[19] D. Soldner and J. Mergheim. Thermal modelling of selective beam melting processes using heterogeneous time step sizes. *Computers & Mathematics with Applications*, 78(7):2183 – 2196, 2019. Simulation for Additive Manufacturing.

[20] I. Yadroitsev, I. Yadroitsava, A. Du Plessis, and E. MacDonald. *Fundamentals of laser powder bed fusion of metals*. Elsevier, 2021.

[21] Z. Yan, W. Liu, Z. Tang, X. Liu, N. Zhang, M. Li, and H. Zhang. Review on thermal analysis in laser-based additive manufacturing. *Optics & Laser Technology*, 106:427 – 441, 2018.

[22] N. Zander, T. Bog, S. Kollmannsberger, D. Schillinger, and E. Rank. Multi-level hp-adaptivity: High-order mesh adaptivity without the difficulties of constraining hanging nodes. *Computational Mechanics*, 55(3):499–517, Feb. 2015.